SSRG International Journal of Electrical and Electronics Engineering
ISSN: 2348-8379/ https://doi.org/10.14445/23488379/IJEEE-V10I1P118

Volume 10 Issue 1, 187-196, January 2023

Original Article

A Novel Deep Learning-Based System for Real-Time Temperature Monitoring of Bone Hyperthermia

Priscilla Whitin[1], V. Jayasankar[2]

[1,2]*Department of EEE, Vel Tech Rangarajan Dr. Sagunthala R&D Institute of Science and Technology, Tamilnadu, India.*

[1]*Corresponding Author : priscillawhitinresearchscholar@gmail.com*

Received: 11 December 2022 Revised: 13 January 2023 Accepted: 21 January 2023 Published: 29 January 2023

Abstract *- High-intensity focused ultrasound is a form of thermal therapy that does not involve any incisions and is used for hyperthermia and removal treatments. Monitoring the temperature is essential for such operations to provide the required quantity of thermal dosage to the target region without causing damage to the strong tissues that are located in the surrounding area. In order to accomplish this goal, a number of different medical imaging approaches have been developed. Magnetic resonance imaging allows temperature readings to be taken with a high degree of precision. Because it does not emit ionizing radiation, is easily accessible, and has a low cost, ultrasound is a medical imaging modality that is regarded favourably for use in temperature monitoring. This is of particular importance in cases involving bone tumors because of the sensitive tissues that are located nearby. Due to the fact that temperature affects both the rapidity of sound and the reduction of ultrasound waves, it is possible to estimate temperature by utilizing the physical features of ultrasound. In this article, we suggest a system that uses ultrasonography and a deep learning methodology to monitor the temperature. During HIFU therapy, the system collects data from the ultrasound channels and alternates between ablation and monitoring phases. It was created with this functionality in mind. During the monitoring phase, the ultrasonic elements in the probe are in charge of receiving ultrasound pulses that have been consecutively sent from the 256 HIFU components. We train a convolutional long short-term memory computational model using ultrasonic data to generate temperature images. Magnetic resonance thermometry readings are compared to the resulting temperature images. The mean and maximum discrepancies between each picture are calculated as a means of gauging the performance of the proposed neural network. This research suggests using a neural network to recreate thermal pictures. For this purpose, we utilize the ultrasound channel data in conjunction with a CLSTM neural network to create temperature pictures. Images of temperatures are compared with those acquired using magnetic resonance thermometry. Because this approach can acquire the progression of temperature from a vast quantity of facts, it may be less sensitive to the placement of the ultrasonic element. Phantom research allowed us to verify the accuracy of the temperature image reconstruction approach. A technique of temperature monitoring that makes use of an external ultrasonic component and deep learning reconstruction appears to be feasible, according to the encouraging findings obtained.*

Keywords *- Temperature, HIFU, Bone tumors, CLSTM, Magnetic resonance.*

1. Introduction

Hyperthermia has significant potential for increasing local control and reducing toxicity in cancer. Mild hyperthermia, the process of heating tumors to temperatures of 40 to 43 degrees Celsius, is the most effective sensitizer for radiation and chemotherapy. Adjuvant hyperthermia stands out because, over a wide range of tumor locations and histology, it either does not increase late toxicity or just slightly increases it. Hyperthermia has a high acceptability and low morbidity, making it possible to retreat with radiation in patients who have previously been substantially preirradiated. It also dramatically improves survival for several 'de Novo' patient groups. Tumor cell death can be accelerated by a number of different pathways, some of which are temperature-dependent. Direct cell death due to hyperthermia is related to temperatures exceeding 42 degrees Celsius. DNA damage repair following chemotherapy or radiation is impeded at temperatures exceeding 40 degrees Celsius. Improving perfusion twitches at a surprisingly low temperature (39°C) makes it one of the most well-known hyperthermia processes. The medical oncology field has noticed the newly discovered molecular understanding of how hyperthermia decreases BRCA2 because it opens the door to novel tactics for combining targeted medicines with hyperthermia. The perceived difficulty in applying good-grade heating is a key obstacle to the clinical employment of HT, irrespective of the promising therapeutic outcomes.

Monitoring temperature with ultrasound (US) that is both accurate and precise can be helpful for various medical therapies. To create physiological changes advantageous to the patient's health, mild hyperthermia requires the tissue temperature to maintain between 39 and 42 degrees. HIFU is typically utilized in the treatment of

cancer [2]. Necrosis is induced by the local heating of tissues using this sort of ultrasound. A number of different techniques have been suggested as potential aids in the monitoring of spatiotemporal shifts in the temperature of tissue in the US [37]. As a result of the fact that temperature shifts are typically not clearly visible in standard B-mode ultrasound pictures, quantitative ultrasound (QUS) approaches have been researched to increase the imaging contrast of temperatures. QUS approaches have been created from various tissue models and use radio-frequency data (obtained before the reconstruction of an ultrasound picture) to estimate parameters linked to various tissues' physical attributes [4].

Locally administering heat to the tumour area constitutes hyperthermia, a form of adjunct cancer handling that boosts the effectiveness of radiation and chemotherapy[11]. In 420 patients with locally advanced cancer, Franckena et al. [10] conducted a retrospective study and found that the chance of cure is connected with the thermal dosage given to them[14]. The study's results demonstrated the need to monitor temperatures carefully and the necessity of maximizing the benefits of thermal exposure. However, despite the fact that intraluminal thermometry is the gold standard for temperature evaluation through therapy, it suffers from significant constraints. It can only provide information from a limited number of places. It is possible that combining an MR-compatible hyperthermia device with MR imaging is the best technology for real-time dosages and quality assurance. This is because it makes it possible to monitor the temperature without causing any damage to the patient. However, its accuracy in the pelvic region is insufficient for real-time thermal dosimetry and is easily disrupted by sound and activity irregularities. The clinic's current non-invasive temperature monitoring options are limited to MR temperature measurements. As a result, there is an urgent need for new advancements to enhance MR thermometry readings and permit thermal dosimetry while therapy is being administered.

Tissue radiodensity is temperature-dependent, with higher temperatures causing a reduction in radiodensity. Therefore, CT-based thermometry, also known as CT numbers or the Hounsfield units (HU), can indirectly be used to monitor tissue temperature changes. However, the volumetric thermal expansion coefficient of the material in question [5] determines the sensitivity (change in HU per degree Celsius). CT-based thermometry has the potential to be used in the monitoring of tissue temperatures during high-frequency treatments or microwave ablation of liver and kidney cancers [7,44]. Despite the existence of such evident connections, the technique has seen limited use in clinical practice thus far [39]. This is because more frequent scans with CT need a larger dose of ionizing radiation, for example, in thermometry [9], and the reproducibility of quantitative CT numerical measures has not been assured. Additional study is necessary to thoroughly investigate the elements that affect CT-based thermometry to be effective.

This research proposes a deep-learning strategy for non-invasive temperature monitoring during HIFU therapy. This monitoring would be done without the need for any intrusive techniques. The DL model that was intended to analyze the microwave fields scattering from a realistic bone phantom was changed to include multiple tumor inclusions with thermal anomalies and hot spots in the healthy tissues around the phantom. The proposed technique does not include retrieving a thermal map but relies on identifying a thermal anomaly. The suggested approach is a DL-based assessment method that has been statistically verified for various situations. So far as the author is aware, this is the first work to use DL on microwave scattering data for thermal monitoring, shifting the focus of semi-research from temperature mapping to thermal surveillance. These two milestones have never before been reached in the history of scientific inquiry, but both have been in the course of this study.

The document portions are structured as follows: The related works for the hyperthermia treatment regarding bone cancer and temperature monitoring are detailed in Section 2. The approach that was used is detailed in section 3. The construction of the deep learning model, and the outcomes of training and evaluation, are all discussed in Section 4. In the last portion, number 5, conclusions are reached.

2. Related Works

Non-invasive and instantaneous detection and monitoring of thermal ablation are essential to significantly improve the clinical implementation of cancer therapy procedures, which is presently challenging due to the dissatisfying functionality of traditional ultrasound scans commonly used in medical training. Deep learning has recently started influencing biological investigations and submissions, using the capacity to integrate massive datasets and join prior knowledge [40]. The use of deep learning methods, and convolutional neural networks, in particular, has improved medical picture processing significantly [12], [13]. Image analysis, classification, object detection and recognition, alignment, artefact restoration, quantization, and rebuilding are just some fields that have benefited from these advancements. Within the scope of this investigation, we investigated and analyzed the practicability of employing a deep CNN framework for thermal lesion identification and monitoring brought about by MWA Features associated with the thermal lesion was detected and maintained using original radiofrequency data backscattered from the ablated area in the United States. This is in contrast to the majority of visual object recognition tasks, which involve dealing with images.

Convolutional neural networks have recently led to inventive outcomes in various tasks, including categorizing images and detecting cancer [15,42]. A pattern of message processing similar to that of the human brain may be imitated using CNN, an artificial neural network. Several convolution channels are used to extract information from

the input data, and the resulting filtered return properties can be used in a classification process. CNNs have also been applied, with significant accuracy levels, to identifying Raman spectra [3,16,17,38].

Medical imaging has benefited from the effective use of deep learning techniques [18-23], which has opened up new possibilities for developing computer-aided diagnostic imaging diagnosis systems (AI). These techniques include segmentation, detection, classification, and enhancement. Effectively applying deep learning methods in orthopedic radiology for lesion diagnosis and severity rating has been a common practice in recent years. Some examples of these lesions include a fracture [24-27], a knee lesion [28,29], osteoarthritis, and a degenerative spinal lesion. In addition, certain models based on deep learning are used to evaluate the age of the bones [30-35] and identify the gender [45] based on radiographs. In light of this, it is feasible to employ deep learning methodologies to build diagnostic models for bone malignancies, which might significantly reduce the rates of misunderstanding and missed diagnosis of bone metastases.

Several recent research has shown the enormous potential of deep learning-based Ai applications in the diagnosis, segmentation, delineation, and visual assessment of bone cancers, resulting in increased diagnostics, predictive, and forecasting accuracy. These models were used to identify bone tumors and classify, segment, and interpret visual data. Furthermore, radionics is an advanced technology that frequently cooperates with artificial intelligence. The goal is to use quantitative characteristics of images, such as shape, shape, surface, and brightness, to isolate radiological patterns that can be analyzed numerically. Constant comparisons to deep learning are made between these two technologies. Even more cutting-edge than genomics is a field called radiomics. It is common knowledge that radiomics has the potential to be utilized in the field of illness diagnosis, prognosis, and monitoring.

3. Methodology

3.1. Mathematical Model of Hyperthermia Treatment

For treatment planning, prediction, and optimization, mathematical modeling is an essential tool. In point of fact, it helps determine the appropriate dose and the quantity of energy communicated, simplifying the analysis of the physiological parameters and monitoring and predicting the therapeutic effects. Solving the bio-heat equation, also known as the Pennes equation, is essential to produce tissue heating. This is the case regardless of the method that is utilized.

$$\rho H \frac{\partial B_T}{\partial \mathrm{t}} = a\nabla^2 B_T + S_i \tag{1}$$

ρ represents the density of the tissue mass which has the unit of kgm^{-3}. H is the heating capacity measured by $Jkg^{-1}k^{-1}$. Variable a, represented by the unit $Wm^{-1}k^{-1}$ represents the heat conductivity and a Representation of the Original Source S_i measured by, Wm^{-3} .

$$S_i = S_s + S_{mh} + S_{hl} \tag{2}$$

S_s represents the source of heat, S_{mh} represents the heat generation, S_{hl} is the loss of heat. The source of heat is electromagnetic heat which is used for the treatment.

$$S_s = \frac{\delta}{2}|EI_0|^2 \tag{3}$$

The electrical conductivity is represented by δ . $|EI_0|^2$ represents the electrical field intensity measured by Vm^{-1}. When the source of heat is constant with time, it can be represented as,

$$\rho H \frac{\partial B_T}{\partial \mathrm{t}} = a\nabla^2 B_T + S_s + S_{hl} \tag{4}$$

It's a simple equation, and it may be used to model the behaviour of a biological system under particular conditions: For one, it disregards the fact that veins also provide heat to the body and implies that all arterial heat is absorbed locally by the tissue; for another, it assumes that arterial temperature is the same as core body temperature.
All of these factors contribute to an inaccurate assessment of blood perfusion, which may be determined using the following formula:

$$S_{hl} = -\omega_{bpr} SH_{bpr} \rho_{bpr} (T - T_{bpr}) \tag{5}$$

What the body's blood supply looks like ω_{bpr} and measurement is by ml$kg^{-1}k^{-1}$. SH_{bpr} represents the specific heat of the human body's blood ($Jkg^{-1}k^{-1}$). For the mass-to-volume ratio of blood, use the symbol ρ_{bpr}. Aortic blood temperature is indicated by the symbol T_{bpr} $[K]$. If the body's temperature rises, blood removes the excess heat, and if it falls, blood transports the lost heat. The negative sign reflects this process of compensating for temperature changes by the blood. Solving the electromagnetic equations (Maxwell's equations) is required to find the bio-heat source term S_s. Since MW wavelengths in tissue are in the cm range, modeling of wave propagation is necessary to account for the conversion of MW energy to heat owing to dielectric losses.

$$\Delta \times M_s = D_s + \frac{\partial D_{ef}}{\partial \mathrm{t}} \tag{6}$$

The magnetic flux density $[Am^{-1}]$ is denoted by the letter M_s. the current concentration is D_s. the density of the flow of electricity is D_{ef} $[Am^{-2}]$. $\frac{\partial D_{ef}}{\partial \mathrm{t}}$ is the concentration of the eddy currents $[Am^{-2}]$. According to the "Maxwell-Faraday equation," variations in the magnetic field F $[V_s m^{-2}]$ have an effect on the electric field E $[V\, m^{-1}]$.

$$\Delta \times E = -\frac{\partial F}{\partial \mathrm{t}} \tag{7}$$

The rules of Gauss for the electric ground and the magnetic field describe the facts that the magnetic arena F does not have any source and that the source for the

electric displacement is the electrical charge density $\rho[A\ s\ m^{-3}]$:

$$\Delta . D = \rho \quad (8)$$

$$\Delta . F = 0 \quad (9)$$

Only when the electromagnetic arena is brought into contact with matter is the latent energy it contains made manifest for human perception (this interaction depends on the ratio between the dimension of the object and the wavelength). To create a model closer to reality, it is essential to consider the fluctuations in temperature caused by physiological thermoregulation, which is determined by the electrical and thermal characteristics of the tissue. Knowing the electrical properties of biological tissues as a function of temperature allows for an accurate determination of the quantity of deposited electromagnetic energy.

3.2. Hyperthermia Treatment for Bone Cancers

Thermotherapy and thermal ablation are the two primary applications of hyperthermia. The goal of thermotherapy is to selectively kill tumor cells without harming the healthy tissue around them by raising the body temperature to between 41 and 45 degrees Celsius. Thermotherapy can also improve the efficacy of other cancer therapies, including radiation and chemotherapy. In contrast, thermal ablation involves subjecting cells to temperatures higher than 45 C. This procedure may harm both tumor and healthy tissue.

It is not known how hyperthermia causes cell death, although it is believed to be the result of several different cellular disturbances. However, hyperthermia causes cells to die via necrosis or apoptosis in the long run. The inflammatory reaction that follows necrosis (premature cell death) is a passive pathogenic process, while apoptosis is a genetically regulated, designed cell death. However, the protein cascades activated during extrinsic and intrinsic apoptosis are distinct, despite the fact that both processes result in cell death. Most apoptosis-inducing stimuli can also produce necrosis if the cell is heated for an extended period of time. Some kinds of cells have been proven to be more susceptible to apoptosis after heat exposure, while necrosis is more likely to occur at specified temperatures.

3.3. HIFU Experimental Setup

A HIFU system and an outside ultrasonic sensor will make up the planned configuration for the setup. The steps of heating and monitoring the temperature are intertwined throughout the operation. A continuous wave, or CW, is emitted by the HIFU components during the combustion stroke to raise the temperature of a specific region. During the monitoring phase of the process, the HIFU components send out ultrasound pulses in sequential order. The external ultrasound sensor was responsible for receiving the ultrasound waves emitted by each HIFU element, which allowed for the measurement of varying flight times during the experiment. We are able to get a high level of prediction accuracy by reconstructing temperature pictures using a neural network. This network requires a significant number of training data sets. It is difficult to acquire adequate data with our innovatively designed technology because of this. We can circumvent this restriction by employing a physics-based HIFU simulation to produce the training data sets. These simulations come with a variety of HIFU powers and ultrasound sensor positions. Thus, we may use data sets derived from simulations to train the network and data sets derived from actual trials to test it.

3.4. Proposed Neural Network Model Design

The ToF that was obtained before the ablation operation and the ToF shifts that occurred during the HIFU procedure are concatenated together to form the network's input. Because the shifted ToF is shorter than the original ToF, we use a millisecond value for the first ToF in the input sequence, and for subsequent ToF changes, we use a microsecond value.

The network's final product is a thermal image, and the MRI's own heat scans serve as reference points for the final picture. Adam is the optimizer that we utilize. The mean square error serves as the loss function, and the learning rate is 0.0005. The picture has a resolution of 1 millimeter × 1 millimeter. In this architecture, the input vector first passes through a series of fully connected networks before reaching the CNN and dropout layers. It involves adding a dropout layer before the final fully connected one and then halving the dropout probability of that layer. Fig.2 depicts the artificial neural network's architecture. The change in TOF shift is necessary to determine the temperature [8]. The CLSTM network has the ability to extract spatial as well as temporal properties from channel data. As an input, we make use of the unprocessed channel data, which includes information about amplitude and TOF. We utilize the data from the time series channel as the input for the CLSTM block; this allows the network to learn how the amplitude and TOF change over various temperature profiles.

3.5. CLSTM Model

The fundamental drawback of FC-LSTM is that it cannot interpret spatiotemporal data since it uses full connections in input-to-state and state-to-state transitions in which no spatial information is recorded. This limitation is the primary reason for the aforementioned limitation. In order to solve this issue, a unique aspect of our design is that all of the inputs $I_1, \ldots, I_t$, cell outputs O_1,..., O_t, hidden states hv_1,..., hv_t, and gates ig_t, fg_t, og_t of the CLSTM are three-dimensional tensors, the last two dimensions of which are the spatial dimensions. It could help to think of the inputs and states of the system as superimposed vectors on a spatial grid to gain a clearer image of the system. For each grid cell, the CLSTM algorithm considers the inputs and past states of its nearest neighbours to predict what that cell will be like in the future. To achieve this, a convolution operator may be used in state-to-state and input-to-state transfers. The primary equations that are

used in CLSTM are presented below. The convolution operator is denoted by ∗t in this equation, and the Hadamard product, denoted by °, is defined before.

The result of the CLSTM algorithm is then used in a convolution operation. Additional input in the form of location vectors is now being sent into the network. Included are the positions of the HIFU elements in reference to the ultrasound element receiving the signal. After passing the vector through a few convolutions and completely connected layers, it is reformatted into a 40×40 array. After going through layers of convolution and transposed convolution, it emerges with a flattened appearance. Fig 1. Shows the overall architecture of the proposed work for temperature monitoring during hyperthermia in bone cancer treatments. In the end, it is molded into a 20×20 picture after being linked to a completely connected layer with 400 size vector yield and being connected to a fully connected layer.

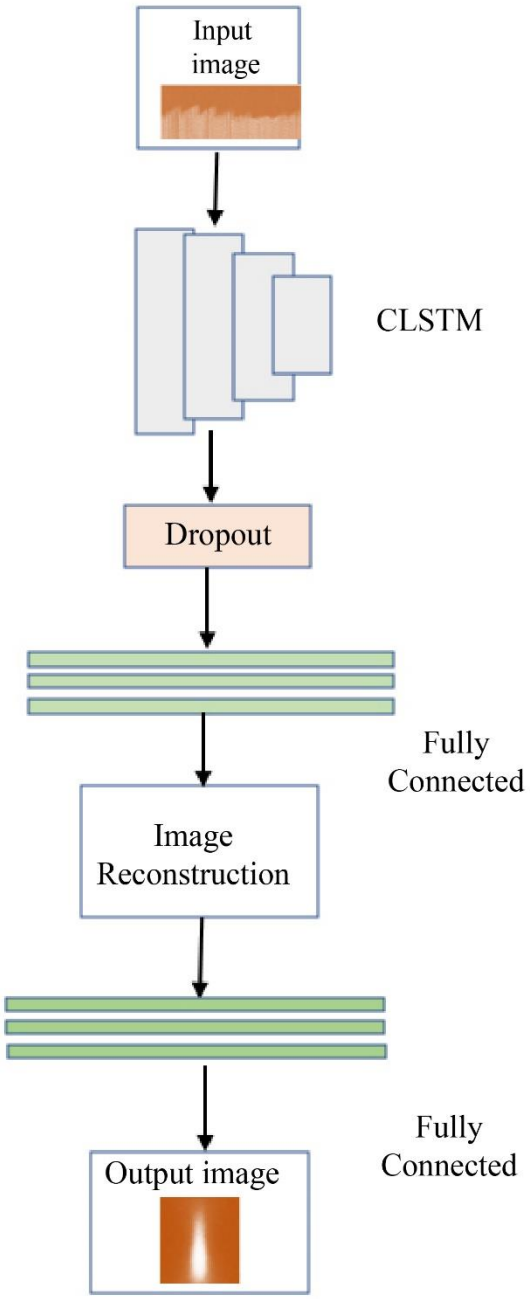

Fig. 1. Overall proposed model architecture

$$ig_t = \sigma\left(W_{iig} * i_t + W_{vig} * V_{t-1} + W_{oig}{}^{\circ}\, O_{t-1} + b_{ig}\right) \quad (10)$$

$$fg_t = \sigma\left(W_{ifg} * i_t + W_{vfg} * V_{t-1} + W_{ofg}{}^{\circ}\, O_{t-1} + b_{fg}\right) \quad (11)$$

$$og_t = fg_t{}^{\circ}\, O_{t-1} + ig_t{}^{\circ} tanh(W_{iog} * i_t + W_{vog} * V_{t-1} b_{og}) \quad (12)$$

$$op_t = \sigma(W_{iop} * i_t + W_{vop} * V_{t-1} + W_{oop}{}^{\circ}\, O_t + b_o) \quad (13)$$

$$V_t = op_t{}^{\circ} tanh(og_t) \quad (14)$$

A CLSTM with a larger transitional kernel should be able to capture faster motions, whereas a CLSTM with a smaller kernel should be able to catch slower motions if we consider the states to be hidden representations of things in motion. To ensure that the output states have the same number of rows and columns as the inputs, padding must be performed before the convolution operation is performed. In this context, padding of the hidden states on boundary points might be seen as an application of the state of the outside world to the computation. In most cases, before the first input arrives, we zero out all of the states of the LSTM, representing "complete ignorance" of the future.

This happens before the first input arrives. When re-creating an output temperature picture, the first fully linked layer expands the size of the output vector to ensure that enough pixels are re-created. The size of the output vector must be bigger than the size of the input vector.

4. Experimental Setup

The system includes a magnetic resonance (MR)-compatible ultrasound probe with 128 components, a 256-element high-intensity focused ultrasound (HIFU) system, and a phantom composed of 2% agarose and 2% silicate minerals to mimic human soft tissue. All of these components are contained within a single housing. In order to facilitate acoustic coupling, the surface of the HIFU is coated in mineral oil and degassed water. In order to gather ultrasound signals, the ultrasound probe is fastened to the holder placed on top of the phantom. This configuration is permanently installed in the MR gantry so that simultaneous MR temperature pictures and ultrasound channel data may be collected.

During the removal phase, the HIFU components send out incessant waves at a power level of 78 Watts for a period of five seconds. The temperature rises as a result of the acoustic wave becoming concentrated at the natural pivotal point. Each HIFU element sends out ultrasonic

pulses in sequence during the monitoring phase, with a power output of 2 Watts and a pinging interval of 3 ms. Because of the fluctuation in temperature, ultrasound waves travel through the target region at varying rates. An ultrasonic probe compatible with magnetic resonance is used to record the pulses. After a delay of 131.072 milliseconds, we capture 4096 samples at a sampling rate of 62.5 megahertz. In the event that the HIFU element diffuses the signal while the sampling is synced with it, a trigger will be produced.

4.1. Dataset

A biophysical model simulates the surface temperature in a three-dimensional volume during the heating phase to create the training data set. This simulation is performed while the HIFU ablation is being performed. The biophysical model parameters are adjusted to closely resemble the experimental setup and the time sequence carried out during the experiments. There are two separate powers, each 50 and 70 Watts. We simulated the experiment for 120 seconds, during which time we generated a temperature volume every second. A conversion curve determined for our agarose phantom is utilized to transform the temperature volumes created into the speed of sound volumes.

Table 1 shows the parameters of the Model during the experimental setup. Time of flight is determined for 150 alternative positions of the external element inside a volume of 26 mm × 8 mm ×1 mm adjacent to the external element location utilized in the experiment. This results in a grand total of 43658 simulated data sets. Different element positions are randomly assigned to validation and training sets. We train with data from 80% of our sites and test with data from the remaining 20%. To train and rebuild, we only employ an axial picture slice that includes the furnace's epicenter.

Table 1. Parameters of the biophysical model during experimental setup

parameters	Value
Power	50 watts and 70 watts
Simulation Time	120 second
agarose phantom	conversion curve
Time of flight (ToF)	150
external element- volume	26 mm × 8 mm ×1 mm
Total data	43658
Train, Test	80%, 20%

5. Performance Evaluation

5.1. Evaluation Metrics

The performance of a model can be determined in large part based on the measure that is used for assessment. Mean absolute error, root mean square error, mean absolute percentage error and correlation coefficient are the four evaluation techniques utilized in this experiment (R). MAE is a range that starts at 0 and goes all the way up to positive infinity, as shown in figure 2. Its value is equal to 0 when the anticipated value and the actual value are an exact match. When the value is reduced, the margin of error also decreases.

$$MAE = \frac{1}{K}\sum_{j=1}^{K}\left|z_j - \hat{z}_j\right| \quad (15)$$

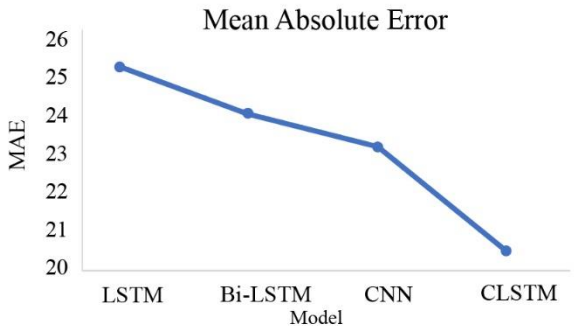

Fig. 2 Performance of a model based on MAE

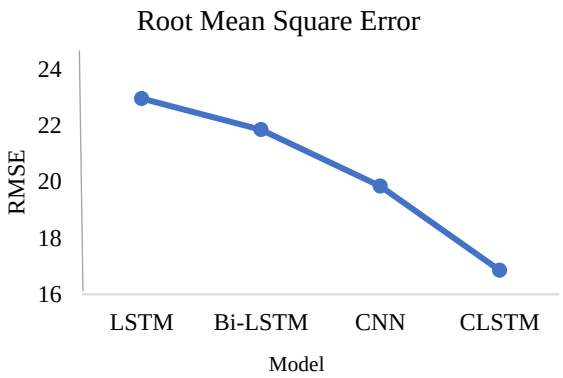

Fig. 3 Performance of a model based on RMSE

Calculating the RMSE involves finding the square root of the quadratic and the observational n ratio of the discrepancy between the observed and expected values. The standard deviation will also be lower when the value is lower, as shown in fig.3.

$$RMSE = \sqrt{\frac{1}{K}\sum_{j=1}^{K}\left(z_j - \hat{z}_j\right)^2} \quad (16)$$

If we take the average absolute error between each observation and the arithmetic mean, we get the absolute deviation of the mean. The mean percentage deviation is another name for this statistic. As can be seen in fig.4, the average absolute error avoids the problem of mistakes cancelling each other out by more accurately reflecting the amount of the true forecast inaccuracy.

$$MAPE = \frac{1}{K}\sum_{j=1}^{K}\frac{\left|zo_j - \widehat{zo_j}\right|}{zo_j} \quad (17)$$

R determines the degree to which the expected and actual values have a linear association. The closer you are to 1, the more significant it is, as shown in fig.5.

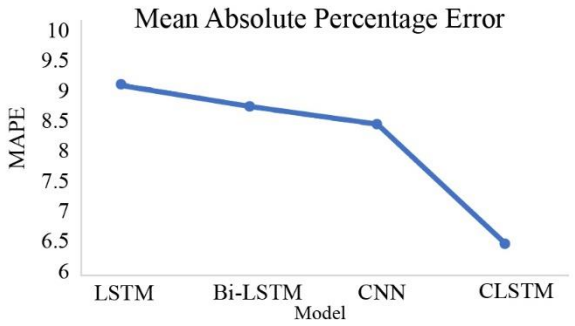

Fig. 4 Performance of a model based on MAPE

$$R = \frac{\sum_{j=1}^{K}(zo_j - \overline{zo_j})(\widehat{zo}_j - \overline{\widehat{zo}_j})}{\sqrt{\sum_{j=1}^{K}(zo_j - \overline{zo_j})^2\,(\widehat{zo}_j - \overline{\widehat{zo}_j})^2}} \quad (18)$$

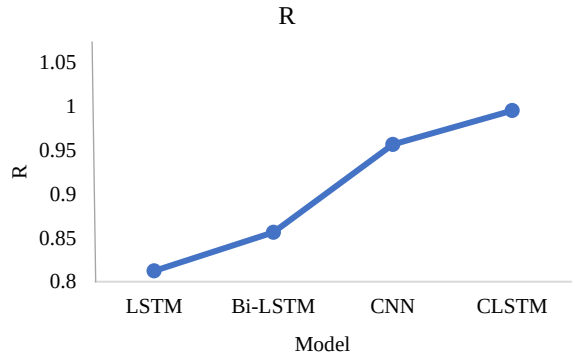

Fig. 5 Performance of a model based on R

The calculations shown above refer to K as the number of samples, z_j as the actual value, $\hat{z}_j$ as the predicted value, $\overline{z_j}$ as the mean of the real value.

The pertinent assessment indicators are also included in Table 2, which may be found here. From the data in the table, it is clear that the single LSTM model has the lowest forecast impact of the four models. It has the most error slots and the least fit effect. Check out the graph for yourself to see the proof. The Bi-LSTM model's predictive power is on par with that of the LSTM model, and it actually improves upon the LSTM model slightly. Out of these four models, the CLSTM has the best prediction effect because of its low Mean square error and root mean squared error values, high R-value, and a high degree of fitting.

Table 2. Performance Evaluation Based on MAE, MAPE, R, RMSE

Model	Mean Absolute Error	Mean Absolute Percentage Error	Root Mean Square Error	R
LSTM	25.3562	9.35	22.9656	0.8123
Bi-LSTM	24.1246	8.96	21.8562	0.8563
CNN	23.2580	8.65	19.8472	0.95.65
CLSTM	20.5246	6.56	16.8542	0.9952

5.2. Accurately Predicting the Slope of the Time-Temperature Relationship (AUC)

The time-temperature records from the HT treatment unit were used in the AUC computation with a sampling interval of 10 s. To do this, we conduct a linear interpolation between the various time t (on the X-axis) and temperature T (on the Y-axis) data points (Y-axis). For a certain trapezoidal section, the area under the curve would be intended as follows for a specific time period, denoted by $t1, t2$, and a temperature difference, denoted by $T1, T2$:

$$The\ area\ under\ the\ curve\ (AUC)$$
$$for\ each\ trapezoidal(T_1 + T_2)(t_1 - t_2) \quad (19)$$

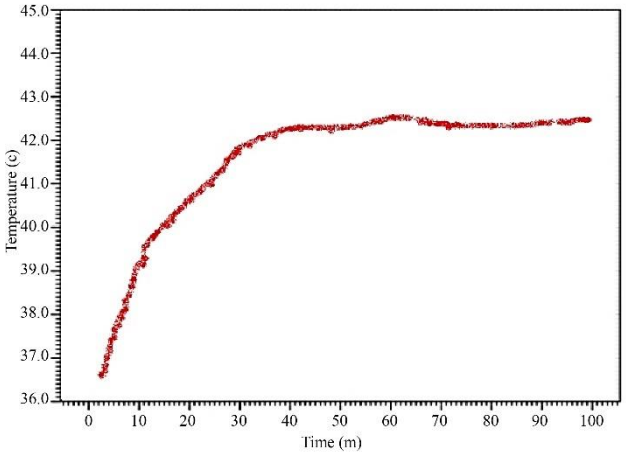

Fig. 6 Time-temperature plot

So, for each HT session, we calculated the total area under the curve (AUC), which includes pre-heating and active heating:

$$AUC \approx \sum_{i=1}^{M}\left(\frac{TE_{M-1}+TE_M}{2}\right)(ti_{M-1} + ti_M) \quad (20)$$

The temperature at the time instant ti_m is represented by the symbol TE_m, , and the temperature at the time of instant $ti_{m-1}$is represented by the symbol TE_{m-1}, where ti represents the time in minutes, and TE indicates the temperature in degrees Celsius. Each temperature reading is accompanied by a discrete-time index beginning with the letter M, and the conclusion of the heating session is similarly denoted by the letter M.

Figure 6 depicts a time-temperature curve from a patient undergoing hyperthermia treatment for urinary bone cancer. During the full 90 minutes of severe hyperthermia, temperature represents the intraluminal temperature in bone taken every 10 seconds.

We used a learning rate of 0.00001 when training the network over the course of 800 epochs. As can be seen in Figure 7, the reconstructed pictures have a dimension of 38 millimeters by 78 millimeters and a pixel size of 1 millimeter by 1 millimeter. They are centered on the area of interest. The size of the output vector is 3,578; however, to reshape the reconstructed pictures, we only need the front 3,444 pixels.

(a) original images, (b) reconstructed images
Fig. 7 Original and reconstructed images

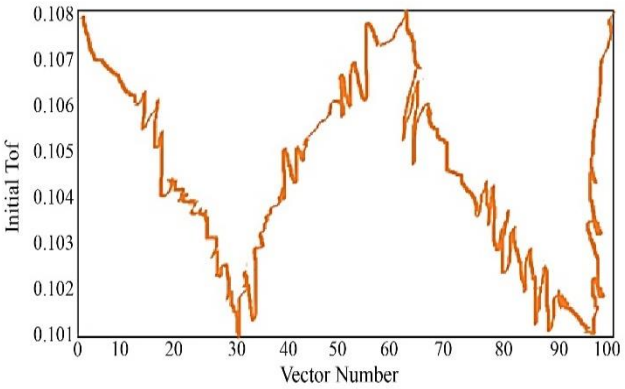

(a) with initial ToF

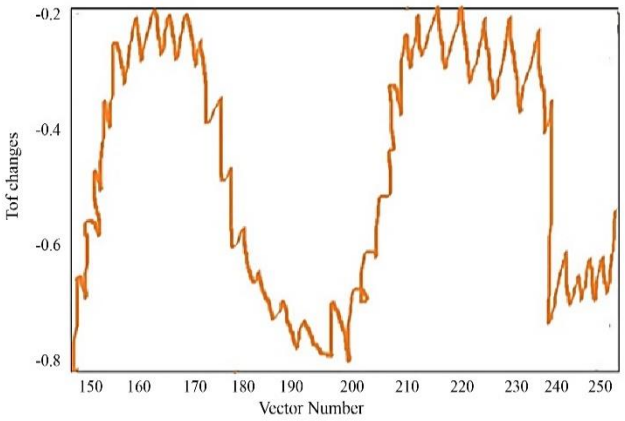

(b) ToF changes
Fig. 8 Shifted the time of flight is appended to the starting time of flight to create the input vector

We were able to obtain mean errors of $0.08 \pm 0.05℃$ and maximum errors of $1.02 \pm 0.52℃$ over the entirety of the validation set when comparing the reconstructed pictures to the original photos. The worst-case scenario was a recreated picture showing an extreme variance of 2.53 degrees Celsius. In Fig. 8, we can see an example of a restored picture based on the endorsement data set, the associated original image, and the images created. Fig. 8 shows the shifted flight time is appended to the starting time to create the input vector. Fig. 9 illustrates the outcomes of our neural network's reconstructive efforts.

In the region of interest (ROI), we determine both the mean and the maximum absolute error for each output picture. The axial picture test set has obtained mean errors of $0.08 \pm 0.05℃$ and maximum errors of $1.02 \pm 0.52℃$ over the entirety of the validation set when comparing the reconstructed pictures to the ground truth photos.

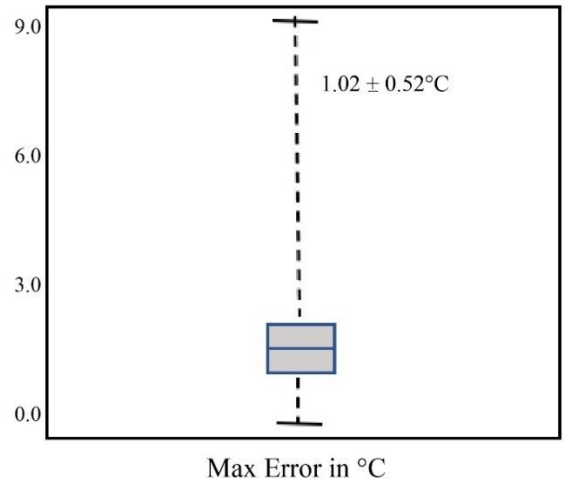

(a)

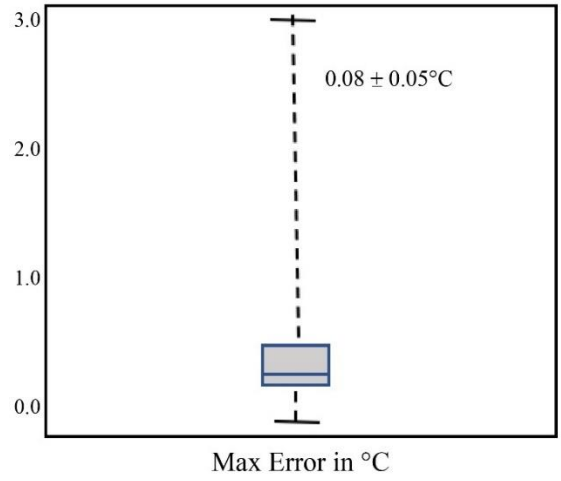

(b)
Fig. 9 Absolute pixel-based inaccuracy in axial pictures taken using the test set: (a) peak error, (b) mean error

6. Conclusion

The Use of Deep Learning to Improve Performance CLSTM is offered as a method for reconstructing temperature images from raw data collected via acoustic channels. Because our technique involves nothing more than positioning the ultrasonic components directly on top of the target, the setup is both straightforward and inexpensive. Experiments are carried out so that data may be gathered and the neural network can be trained. The findings indicate that the suggested approach of ultrasound thermometry for HIFU therapy monitoring, which uses ultrasound channel data and deep learning, is technically feasible. Because the method uses ultrasound data recorded before eradication, patient mobility is a challenge because the channel data acquired at the starting state would be diverse from the one in our network. The patient's heart rate can't fluctuate too much because this technique employs ultrasound data from the beginning. The current temperature information before patient mobility and the comparable ultrasonic data change that happens after patient motion will be used in the future as input, eliminating the necessity for initial channel data.

The very limited data storage space is one of this investigation's shortcomings. The upcoming effort will entail collecting additional data for training and validation purposes. More information will be gathered using a variety of biological tissues and distinct element placements. Experiments will need to be carried out in the not-too-distant future to validate the approach. We trust that the accuracy may be enhanced even further by adjusting the hyperparameters and changing the neural network's topology by using more data. Since it is difficult to obtain a sufficient amount of data in adequate quantity, simulation is another option that might be explored. It is possible that we will be able to train the system using information obtained from both simulation and experiments.

References

[1] T. Kujawska et al., "Annular Phased Array Transducer for Preclinical Testing of Anti-Cancer Drug Efficacy on Small Animals," *Ultrasonics*, vol. 76, pp. 92-98, 2017. *Crossref*, https://doi.org/10.1016/j.ultras.2016.12.008

[2] G. Litjens et al., "A Survey on Deep Learning in Medical Image Analysis," *Medical Image Analysis*, vol. 42, pp. 60-88, 2017. *Crossref*, https://doi.org/10.1016/j.media.2017.07.005

[3] K. Prema, and A. Kumar Kombaiya, "An Unsupervised Deep Feature Selection and Ensemble Deep Learning Model for Cancer Classification," *International Journal of Engineering Trends and Technology*, vol. 70, no. 9, pp. 20-33, 2022. *Crossref*, https://doi.org/10.14445/22315381/IJETT-V70I9P203

[4] S. Song et al., "Monitoring Microwave Ablation Using Ultrasound Homodyned K Imaging Based on the Noise-Assisted Correlation Algorithm: an Ex Vivo Study," *Ultrasonics*, vol. 110, p. 106287, 2021. *Crossref*, https://doi.org/10.1016/j.ultras.2020.106287

[5] F. Fani et al., "CT-Based Thermometry: an Overview," *International Journal of Hyperthermia : The Official Journal of European Society for Hyperthermic Oncology, North American Hyperthermia Group*, vol. 30, no. 4, pp. 219-227, 2014. *Crossref*, https://doi.org/10.3109/02656736.2014.922221

[6] Mohammed Saad Alqahtani, "Primary Hemophagocytic Lymphohistocytosis in Adult Woman; A Case Report," *SSRG International Journal of Medical Science*, vol. 4, no. 4, pp. 1-3, 2017. *Crossref*, https://doi.org/10.14445/23939117/IJMS-V4I4P101

[7] P. Bruners et al., "Multi-Slice Computed Tomography: a Tool for Non-Invasive Temperature Measurement?," *International Journal of Hyperthermia : The Official Journal of European Society for Hyperthermic Oncology, North American Hyperthermia Group*, vol. 26, no. 4, pp. 359-365, 2010. *Crossref*, https://doi.org/10.3109/02656731003605654

[8] Ngwobia Peter Agwu, and Ahmed Mohammed Umar, "The Role of Bisphosphonates in the Management of Bone Metastasis," *SSRG International Journal of Medical Science*, vol. 7, no. 10, pp. 5-11, 2020. *Crossref*, https://doi.org/10.14445/23939117/IJMS-V7I10P102

[9] D. Kokuryo, E. Kumamoto, and K. Kuroda, "Recent Technological Advancements in Thermometry," *Advanced Drug Delivery Reviews*, vol. 163-164, pp. 19-39, 2020. *Crossref*, https://doi.org/10.1016/j.addr.2020.11.001

[10] M. Franckena et al., "Hyperthermia Dose-Effect Relationship in 420 Patients with Cervical Cancer Treated with Combined Radiotherapy and Hyperthermia," *European Journal of Cancer*, vol. 45, no. 11, pp. 1969-1978, 2009. *Crossref*, https://doi.org/10.1016/j.ejca.2009.03.009

[11] P. Nishaa et al., "Giant Cell Tumour of the Sternum-Two Cases," *SSRG International Journal of Medical Science*, vol. 3, no. 3, pp. 1-3, 2016. *Crossref*, https://doi.org/10.14445/23939117/IJMS-V3I3P101

[12] G. Litjens et al., "A Survey on Deep Learning in Medical Image Analysis," *Medical Image Analysis*, vol. 42, no. 7, pp. 60-88, 2017. *Crossref*, https://doi.org/10.1016/j.media.2017.07.005

[13] Justin Ker et al., "Deep Learning Applications in Medical Image Analysis," *IEEE Access*, vol. 6, pp. 9375-9389, 2018, *Crossref*, https://doi.org/10.1109/ACCESS.2017.2788044

[14] Dr. Shobha Gusain, "Modifiable Risk Factors for Breast and Cervical Cancer and Their Association with Sample Characteristics," *SSRG International Journal of Nursing and Health Science*, vol. 6, no. 1, pp. 10-16, 2020. *Crossref*, https://doi.org/10.14445/24547484/IJNHS-V6I1P102

[15] V. Gulshan et al., "Development and Validation of a Deep Learning Algorithm for Detection of Diabetic Retinopathy in Retinal Fundus Photographs," *Jama*, vol. 316, no. 22, pp. 2402-2410, 2016. *Crossref*, https://doi.org/10.1001/jama.2016.17216, 2016

[16] Diego Ardila et al., "End-To-End Lung Cancer Screening with Three-Dimensional Deep Learning on Low-Dose Chest Computed Tomography," *Nature Medicine*, vol. 25, pp. 954-961, 2019. *Crossref*, https://doi.org/10.1038/s41591-019-0447-x

[17] K. Munir et al., "Cancer Diagnosis Using Deep Learning: a Bibliographic Review," *Cancers*, vol. 11, no. 9, p. 908873, 2019. *Crossref*, https://doi.org/10.3390/cancers11091235

[18] R. Raman et al., "Fundus Photograph-Based Deep Learning Algorithms in Detecting Diabetic Retinopathy," *Eye*, vol. 33, no. 1, pp. 97–109, 2019. *Crossref*, https://doi.org/10.1038/s41433-018-0269-y

[19] P. Schelb et al., "Classification of Cancer at Prostate MRI: Deep Learning Versus Clinical PI-RADS Assessment," *Radiology*, vol. 293, no. 3, pp. 607–17. 2019. *Crossref*, https://doi.org/10.1148/radiol.2019190938

[20] S. Wang et al., "Predicting EGFR Mutation Status in Lung Adenocarcinoma on Computed Tomography Image Using Deep Learning," *European Respiratory Journal*, vol. 53, no. 3, p. 1800986, 2019. *Crossref*, https://doi.org/10.1183/13993003.00986-2018

[21] Y. Xu et al., "Deep Learning Predicts Lung Cancer Treatment Response from Serial Medical Imaging," *Clinical cancer research : an official journal of the American Association for Cancer Research*, vol. 25, no. 11, pp. 3266-3275, 2019. *Crossref*, https://doi.org/10.1158/1078- 0432.Ccr-18-2495

[22] S. H. AlDubayan et al., "Detection of Pathogenic Variants with Germline Genetic Testing Using Deep Learning vs Standard Methods in Patients with Prostate Cancer and Melanoma," *Jama*, vol. 324, no. 19, pp. 1957-1969, 2020. *Crossref*, https://doi.org/10.1001/ jama.2020.20457

[23] W. Bulten et al., "Automated Deep-Learning System for Gleason Grading of Prostate Cancer Using Biopsies: a Diagnostic Study," *Lancet Oncology*, vol. 21, no. 2, pp. 233-241, 2020. *Crossref*, https://doi.org/10.1016/s1470-2045(19)30739-9

[24] S. W. Chung et al., "Automated Detection and Classification of the Proximal Humerus Fracture by Using Deep Learning Algorithm," *Acta Orthopaedica*, vol. 89, no. 4, pp. 468-473, 2018. *Crossref*, https://doi.org/10.1080/ 17453674.2018.1453714

[25] D. H. Kim, and T. MacKinnon, "Artificial Intelligence in Fracture Detection: Transfer Learning from Deep Convolutional Neural Networks," *Clinical radiology*, vol. 73, no. 5, pp. 439-445, 2018. *Crossref*, https://doi.org/10.1016/j.crad.2017.11.015

[26] N. Tomita et al., "Deep Neural Networks for Automatic Detection of Osteoporotic Vertebral Fractures on CT Scans," *Computers in Biology and Medicine*, vol. 98, pp. 8-15, 2018. *Crossref*, https://doi.org/10.1016/j.compbiomed.2018.05.011

[27] C. T. Cheng et al., "Application of a Deep Learning Algorithm for Detection and Visualization of Hip Fractures on Plain Pelvic Radiographs," *European Radiology*, vol. 29, no. 10, pp. 5469-5477, 2019. *Crossref*, https://doi.org/10.1007/s00330-019-06167-y

[28] I. Š tajduhar et al., "Semi-Automated Detection of Anterior Cruciate Ligament Injury from MRI," *Computer Methods and Programs in Biomedicine*, vol. 140, pp. 151-164, 2017. *Crossref*, https://doi.org/10.1016/j.cmpb.2016.12.006

[29] N. Bien et al., "Deep-Learning Assisted Diagnosis for Knee Magnetic Resonance Imaging: Development and Retrospective Validation of MRNet," *PloS Med*, vol. 15, no. 11, p. e1002699. 2018. *Crossref*, https://doi.org/10.1371/journal.pmed.1002699

[30] C. Spampinato et al., "Deep Learning for Automated Skeletal Bone Age Assessment in X-Ray Images," *Medical Image Analysis*, vol. 36, pp. 41–51, 2017. *Crossref*, https://doi.org/10.1016/j.media.2016.10.010

[31] S. Koitka et al., "Ossification Area Localization in Pediatric Hand Radiographs Using Deep Neural Networks for Object Detection," *PloS One*, vol. 13, no. 11, pp. 0207496. 2018. *Crossref*, https://doi.org/10.1371/journal.pone.0207496

[32] D. B. Larson et al., "Performance of a Deep-Learning Neural Network Model in Assessing Skeletal Maturity on Pediatric Hand Radiographs," *Radiology*, vol. 287, no. 1, pp. 313-322, 2018. *Crossref*, https://doi.org/10.1148/radiol.2017170236

[33] C. Tong et al., "A Deep Automated Skeletal Bone Age Assessment Model with Heterogeneous Features Learning," *Journal of Medical Systems*, vol. 42, no. 12, pp. 249, 2018. *Crossref*, https://doi.org/10.1007/s10916-018-1091-6

[34] X. Ren et al., "Regression Convolutional Neural Network for Automated Pediatric Bone Age Assessment From Hand Radiograph," *IEEE Journal of Biomedical and Health Informatics*, vol. 23, no. 5, pp. 2030–8, 2019. *Crossref*, https://doi.org/10.1109/jbhi.2018.2876916

[35] Y. Gao et al., "Bone Age Assessment Based on Deep Convolution Neural Network Incorporated with Segmentation," *International Journal of Computer Assisted Radiology and Surgery*, vol. 15, no. 12, pp. 1951–62, 2020. *Crossref*, https://doi.org/10.1007/s11548-020-02266-0

[36] Sneha Iyer et al., "In Silico Drug Designing And Phytochemicals Prospect In Liver Cancer Therapeutics," *International Journal of Biotech Trends and Technology*, vol. 11, no. 3, pp. 31-41, 2021. *Crossref*, http://ijbttjournal.org/archives/ijbtt-v11i3p605

[37] R. Righetti et al., "Elastographic Characterization of HIFU-Induced Lesions in Canine livers," *Ultrasound in Medicine & Biology*, vol. 25, no. 7, pp. 1099-1113, 1999.

[38] Debanjoy Paul et al., "Computer-Aided And Herbal Informatics Based Drug Designing for Potential Lung Cancer Therapeutics," *International Journal of Biotech Trends and Technology*, vol. 11, no. 3, pp. 8-17, 2021. *Crossref*, https://doi.org/10.14445/22490183/IJBTT-V11I3P602

[39] S. J. S. Ruiter, W. J. Heerink, and K. P. de Jong, "Liver Microwave Ablation: a Systematic Review of Various FDA-Approved Systems," *European Radiology*, vol. 29, pp. 4026–4035, 2019. *Crossref*, https://doi.org/10.1007/s00330-018-5842-z

[40] Chensi Cao et al., "Deep Learning and Its Applications in Biomedicine," *Genomics Proteomics Bioinformatics*, vol. 16, no. 1, pp. 17-32, 2018.

[41] M. Aruna, S. Sukumaran, and V. Srinivasan, "Hybridization of Fuzzy Label Propagation and Local Resultant Evidential Clustering Method for Cancer Detection," *International Journal of Engineering Trends and Technology*, vol. 70, no. 9, pp. 34-46, 2022. *Crossref*, https://doi.org/10.14445/22315381/IJETT-V70I9P204

[42] D. S. Kermany et al., "Identifying Medical Diagnoses and Treatable Diseases by Image-Based Deep Learning," *Cell*, vol. 172, no. 5, pp. 1122–1131.e1129, 2018. *Crossref*, https://doi.org/10.1016/ j.cell.2018.02.010

[43] Ijaz Sheik et al., "Current Review on Nanoparticles Targeting Colorectal Cancer," *International Journal of Biotech Trends and Technology*, vol. 12, no. 3, pp. 8-17, 2022. *Crossref*, https://doi.org/10.14445/22490183/IJBTT-V12I3P602

[44] Jijo Paul, Thomas J. Vogl, and Annamma Chacko, "Dual-Energy Computed Tomography Thermometry During Hepatic Microwave Ablation in an Exvivo Porcine Model," *European Journal of Medical Physics*, vol. 31, pp. 683–691, 2015. *Crossref*, https://doi.org/10.1016/j.ejmp.2015.05.014

[45] Sehyo Yune et al., "Beyond Human Perception: Sexual Dimorphism in Hand and Wrist Radiographs Is Discernible by a Deep Learning Model," *Journal of Digit Imaging*, vol. 32, no. 4, pp. 665– 71, 2019. *Crossref*, https://doi.org/10.1007/s10278-018-0148-x